Debonding-on-demand Fe_3O_4-epoxy adhesively bonded dissimilar joints via electromagnetic induction heating

Caglar, Hasan; Aksoy, Y. Altay; Idapalapati, Sridhar; Caglar, Baris; Sharma, Mohit; Kerm Sin, Chian

DOI
10.1080/00218464.2023.2256670

Publication date
2023

Document Version
Final published version

Published in
Journal of Adhesion

The Journal of Adhesion

ISSN: (Print) (Online) Journal homepage: https://www.tandfonline.com/loi/gadh20

Debonding-on-demand Fe_3O_4-epoxy adhesively bonded dissimilar joints via electromagnetic induction heating

Hasan Caglar, Y. Altay Aksoy, Sridhar Idapalapati, Baris Caglar, Mohit Sharma & Chian Kerm Sin

To cite this article: Hasan Caglar, Y. Altay Aksoy, Sridhar Idapalapati, Baris Caglar, Mohit Sharma & Chian Kerm Sin (13 Sep 2023): Debonding-on-demand Fe_3O_4-epoxy adhesively bonded dissimilar joints via electromagnetic induction heating, The Journal of Adhesion, DOI: 10.1080/00218464.2023.2256670

To link to this article: https://doi.org/10.1080/00218464.2023.2256670

THE JOURNAL OF ADHESION
https://doi.org/10.1080/00218464.2023.2256670

Taylor & Francis
Taylor & Francis Group

Debonding-on-demand Fe_3O_4-epoxy adhesively bonded dissimilar joints via electromagnetic induction heating

Hasan Caglar[a,b], Y. Altay Aksoy[c], Sridhar Idapalapati[a], Baris Caglar[c], Mohit Sharma[b], and Chian Kerm Sin[a]

[a]School of Mechanical and Aerospace Engineering, Nanyang Technological University, Singapore, Singapore; [b]Institute of Materials Research and Engineering, Agency for Science, Technology and Research (A*STAR), Singapore, Singapore; [c]Aerospace Manufacturing Technologies, Faculty of Aerospace Engineering, Delft University of Technology, Delft, Netherlands

ABSTRACT

We investigated the debonding on-demand (DoD) of adhesively bonded hybrid dissimilar joints by applying electromagnetic induction heating to the joint overlap section, wherein the epoxy resin is reinforced with iron oxide (Fe_3O_4) particles. Ti-6Al-4 V adherends were bonded with CFRP or GFRP adherends using neat/modified epoxy adhesive. DoD tests revealed that eddy current heating of Ti-6Al-4 V was a dominant heating mechanism of the joints while both eddy current and magnetic hysteresis of CFRP and Fe_3O_4 acted as a secondary heating factor. A low content Fe_3O_4 and thinner composite adherend reduced the time to failure of the joints. Likewise, CFRP required a shorter time for debonding compared to GFRP due to its electromagnetic properties. Modifications with 2 and 5 wt.% Fe3O4 for CFRP and GFRP joints led to 31% and 37% time reduction which will be crucial for energy-saving when debonding large structures. Remarkably, sandblasting improved the electromagnetic induction capabilities of Ti-6Al-4 V, leading to a notable increase in the heating rate, which jumped from around 20°C/s to 80°C/s. Sandblasting enhanced the surface roughness of the adherends but only the water contact angle of GFRP decreased considerably. Fe_3O_4 modifications increased the epoxy residue on the Ti-6Al-4 V surface from 26% to 99%. DIC revealed the strain distribution of bulk materials to understand the thermomechanical mismatches between the materials and the adhesive joints exhibited high peel stresses at the overlap ends. The low weight content (2 and 5 wt.%) of Fe_3O_4 exhibited beneficial effects on the mechanical, thermal, thermomechanical, wettability and lap shear strength.

ARTICLE HISTORY
ARTICLE HISTORY Received 23 May 2023
Accepted 4 September 2023

KEYWORDS
Debonding-on-demand; electromagnetic induction heating; epoxy; Fe_3O_4

1. Introduction

Structural adhesives are extensively used to bond similar/dissimilar materials in different industries such as aerospace, automotive and wind energy to realise complex components. Epoxy (non-magnetic) and polyurethane are

CONTACT Sridhar Idapalapati msridhar@ntu.edu.sg School of Mechanical and Aerospace Engineering, Nanyang Technological University, 50 Nanyang Avenue, 639798, Singapore, Singapore
Supplemental data for this article can be accessed online at https://doi.org/10.1080/00218464.2023.2256670

the most preferred adhesives for structural applications and the epoxy market is expected to double in the next 5 years.[1] Although adhesive bonding is widely accepted by various industries, there are some critical issues in adhesive bonding applications. A careful selection of adhesives is required to prevent detrimental issues, especially for dissimilar joint applications (typically polymer composites (carbon fiber reinforced polymers (CFRP), glass fiber reinforced polymer (GFRP)) and metal (Ti-6Al-4 V, aluminium)). This is particularly important for applications like LEAP® Engine blades (3D-woven composite and titanium alloy) by CFM International as mentioned in.[2] Otherwise, the mismatch between the substrates' thermomechanical and physical properties might reduce the strength of the joints significantly. These mismatches can lead to kissing bonds or weak bonds in dissimilar joints.[3] Another important issue is their negative impact on the circular economy and decarbonization due to their incapability of proper disassembly. Thus, an environmentally friendly design for debonding the joints is required to enhance the reusability and recyclability of the bonded materials, especially for those used in end-of-life vehicles. For example, two 10-year-old Boeing 787 were disassembled because they required high maintenance costs.[4]

There are different approaches to enable debonding adhesive joints such as applying thermal, electrical, magnetic, ultrasonic, chemical stimuli or mechanical separation.[1] Anwar et al.[5] examined the effects of high-energy nanosecond laser pulses with wavelengths of 1064 nm and 532 nm on aluminium joints bonded with transparent polymethyl methacrylate (PMMA) polymer for joint debonding with localised heating. The Al surface was analysed before and after subjecting to laser energy, confirming that debonding occurred due to surface melting, which caused minimal alterations to the Al surface. However, a major limitation of this technique is that one of the materials being bonded must be transparent to the laser wavelength, while the other material must be an absorbing metal. Electromagnetic induction heating is a promising technique due to its low energy consumption and local heating capability. A high electromagnetic frequency field induces heat generation by eddy current (i.e., Joule) and/or magnetic hysteresis depending on the material's magnetic and electrical conductivity properties. Iron oxide (Fe_3O_4, i.e. magnetite) particles were integrated to improve the disassembly characteristics by exploiting their electromagnetic properties, cost-effectiveness, reusability and recyclability.[6] The authors reported 19.3% strength enhancement after the addition of particles and 96.3% strength reduction after 3 minutes of dielectric heating. Despite their local heating capabilities by hysteresis, iron oxide particles require a high magnetic field and their heating capabilities are easily influenced by the physical (e.g. thickness) and magnetic (e.g. magnetic permeability) properties of the substrates. A recent study by Sánchez-Romate et al.[7] investigated the synergistic effects of thermally expandable particles (TEPs) and iron oxide (Fe_3O_4) on epoxy adhesively bonded GFRP joints. The

inclusion of TEPs enhanced the heating efficiency (from a slight to moderate level) by improving the dispersion of Fe_3O_4. However, TEPs caused a significant reduction of more than 30% in the lap shear strength at room temperature conditions. Piazza et al.[8] have demonstrated that the thermally expandable particle (TEP) loaded adhesive affects the mechanical properties and debondability of epoxy-bonded single lap joints (SLJs) made of aluminium 6061 and woven carbon fiber reinforced plastic. When the joint overlap area is heated under an electrically charged RF coil, the volumetric expansion of TEPs weakened the adhesive, leading to joint debonding around 100 N. In two recent studies,[9,10] rebonding properties of various thermoplastic adhesives with Fe_3O_4 particles were investigated using single lap joint and disk-shape geometries, respectively.

Digital image correlation (DIC) is a technique for tracking local displacement fields and strain in the mechanical testing of materials. DIC measurements have various applications such as studying the fatigue failure behaviour of CFRP/Al joints,[11] the shear nonlinearities of nanocomposites[12] and the cohesive zone length measurements.[13] In adhesive joints, DIC can monitor the full field surface strain distribution on the joints and predict the strength of the joints.[14,15]

In this study, a two-part paste epoxy adhesive was used to bond the CFRP or GFRP (with varying thicknesses) with Ti-6Al-4 V. Although a few studies considered Fe_3O_4 for debonding of adhesive joints via electromagnetic induction heating, to the best of our knowledge, there is no available study is on debonding Fe_3O_4-modified structural adhesively bonded dissimilar joints while preserving/enhancing the lap shear strength at service temperatures. The effects of electromagnetic induction heating on debonding of the epoxy adhesively bonded joint (that exhibits a crosslinked structure inhibiting the debonding process) were investigated. This study included the following investigations: (i) thermal/thermomechanical characterizations of the materials, (ii) bulk sample characterization, (iii) surface roughness and contact angle measurements before and after sandblasting, (iv) single lap joint tests and (v) in-situ electromagnetic induction heating test under a static load of the lap joints.

2. Experimental materials and procedures

2.1. Materials

High purity (about 99.5+%) 15–20 nm size near-spherical (see Figure 1) iron oxide (Fe_3O_4) particles (supplied by US Research Nanomaterials) were used in this work[16] as this size range show superparamagnetic behaviour.[17] The chemical composition of the powder in ppm is Cr (2) – Co (35) – Na (55) – Mn (39) – Ni (16) – Mg (2) – Al (4.78) – Fe_3O_4 (99.5%) and its true density is

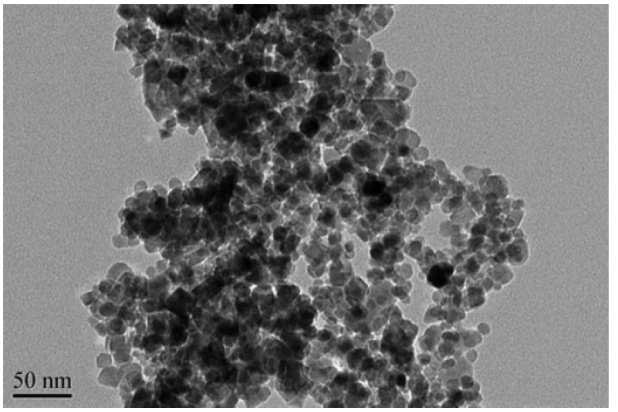

Figure 1. TEM micrograph showing the morphology of iron oxide (Fe_3O_4) particles[16].

in the range of 4.8–5.1 g/cm^3.[16] As a ferrimagnetic material, Fe_3O_4 particles have a Brunauer – Emmett–Teller (BET) surface area of 81.98 m^2/g which has a positive correlation with the magnetization of the nanoparticles.[18] In our specific case, Fe_3O_4 particles gain superparamagnetic properties under 20 nm size.

A high strength, toughness, and temperature resistance two-part epoxy (supplied by 3 M™) Scotch-Weld™ DP490 was used as an adhesive with properties listed in Table 1.

Unidirectional glass fiber reinforced epoxy prepregs of areal density 175 g/m^2 (G17500 supplied by Weihai GuangWei Composites Co., Ltd, China) were stacked to manufacture GFRP laminates. These prepregs have 33% ± 3% epoxy resin, 66% of fiber with less than 1% volatile substance by weight and their mechanical properties are listed in Table 2.

HexPly® M21 (Hexcel) woven carbon prepreg was used to manufacture CFRP adherends, whose properties are provided in Table 3. This prepreg has excellent toughness and high residual compression strength after impact. Both GFRP and CFRP laminates of required thickness were cured as per the suppliers' recommended curing cycle.

Table 1. The material properties of DP490 epoxy adhesive.[19].

Temperature	-55°C	23°C	80°C	120°C	150°C
Shear strength (longitudinal) (MPa)	23.7	30.2	11.9	2.8	1.9
Shear strength (transverse) (MPa)	31.6	28.7	12.7	3.2	1.7
Peel strength (DaN/cm)	-	9.24	7.32	-	-

Table 2. Mechanical properties of unidirectional GFRP laminates.[20].

Young's modulus (GPa)	Shear modulus (GPa)	Tensile strength (MPa)	Compressive strength (MPa)	Poisson's ratio	Density (kg/m^3)
46	7.0	950	700	.26	2200

Table 3. The material properties of HexPly® M21.

Young's modulus (GPa)	Tensile strength (MPa)	Compression modulus (GPa)	Compression strength (MPa)	In-plane shear modulus (GPa)	In-plane shear strength (MPa)	ILSS (MPa)	CAI @ 30.0 J	Tg (°C)	Density (g/cm^3)
73.9	880	63.9	820	4.8	94	70	270	195	1.59

Grade 5 Ti-6Al-4V sheets of 0.5 mm thick, were sourced from William Gregor Ltd, UK and their mechanical properties are listed in Table 4.

Table 4. Supplier provided material properties of Ti-6Al-4 V (where L-longitudinal and T-transverse).

Young's modulus (GPa)	Tensile strength (MPa)	Yield strength (0.2%) (MPa)	% Elongation	Chemical composition
117	963 (L) – 971 (T)	937 (L) – 900 (T)	11.1 (L) – 10.7 (T)	C (.009) - N (.004) - Fe (.2) -Al (6.13) - V (3.88) - O (.15) - Y (<50 PPM)

2.2. Experimental methods

To prepare the adhesive mixture, the epoxy resin and Fe_3O_4 particles were accurately measured using a milligram-sensitive electronic balance. The two components were then mixed together in a planetary mixer (SK-300SII, Kakuhunter) at 2000 rpm for 120 s. Subsequently, the mixture underwent degassing at 2200 rpm for 30 s to remove any entrapped air. Next, the Fe_3O_4-epoxy resin mixture was combined with the hardener in 2:1 ratio in the mixer, blending at 2000 rpm for 240 s, followed by another degassing step at 2200 rpm for 60 s. The resulting adhesive samples were manufactured with Fe_3O_4 concentrations of 0 wt.%, 2 wt.%, 5 wt.%, and 10 wt.% for further characterization and testing purposes. The adhesive mixture was vacuumed for 900 s to remove any entrapped air. The samples were then placed on silicone moulds, specifically used for testing the thermomechanical properties. Cure was achieved by allowing the samples to cure at room temperature for 24 hrs, followed by a heating step at 80°C for 1 hr in an oven.

The adherend preparation process involved several sequential steps for effective bonding. First, the overlapping region of the adherends was sandblasted with 80 grit size aluminium oxide (Al_2O_3) particles to enhance surface roughness and mechanical interlocking. Subsequently, thorough rinsing under running water removed any residual particles, followed by gentle drying with a paper towel. Complete drying was achieved by placing the adherends in an oven at 60°C for 30 min. Next, the sandblasted surfaces were cleaned with acetone to eliminate contaminants, and a brief air-drying period ensured a clean and dry surface. To maintain a consistent bondline thickness, thin stainless-steel spacers (0.2 mm thick) were inserted between the top and bottom

adherends. Finally, the joints were cured by allowing them to cure at room temperature for 24 hrs, followed by heating at 80°C for 1 hr in an oven using 3 LEAP® DP490 adhesive.

The glass transition temperature (T_g), storage modulus (E') and loss tangent ($\tan\delta$) of CFRP were determined using a dynamic mechanical analyser (DMA Q800, TA Instruments) at a heating rate of 5°C/min and a frequency of 1 Hz as described in reference.[21] The same method was applied to obtain E' and $\tan\delta$ values of Ti-6Al-4 V, GFRP and Fe_3O_4-epoxy samples between 40°C and 150°C at a heating rate of 10°C/min. Glass-transition temperature (T_g) of the Fe_3O_4-epoxy samples was measured using differential scanning calorimetry (DSC Q200, TA Instruments) at a heating rate of 20°C/min. The through-thickness thermal diffusivity of the CFRP, Ti-6Al-4 V and Fe_3O_4-epoxy samples at room temperature was measured using ai-Phase Mobile M3 type (ai-Phase Co. Ltd.). Thermo-mechanical analyser (TMA Q400, TA Instruments) was used to measure the through-thickness coefficient of thermal expansion (CTE). The test sample of 6 mm diameter size were heated from an initial temperature of 40°C to a final temperature of 140°C at 10°C/min under small compressive force of 0.05N. By monitoring the dimensional changes of the samples, the through-thickness coefficient of thermal expansion (CTE) was determined. The in-plane coefficient of thermal expansion (CTE) of the individual materials, along with the surface roughness and water contact angle of CFRP and Ti-6Al-4 V, were assessed in accordance with the methodology described in our previous study.[22]

The Contoured Double-Cantilever Beam (CDCB) tests were conducted to measure the adhesive fracture energy using, G_{IC}, using symmetrical 25.4 mm wide aluminium adherends test materials according to ASTM D3433.[23] The tensile properties of plastics and Ti-6Al-4 V were characterized by conducting uniaxial tensile tests on dog-bone samples as per ASTM D638 and ASTM E8, respectively.[24,25] GFRP and CFRP samples were manufactured in the Type I geometry (overall length: 165 mm), while epoxy samples were fabricated in the Type IV geometry (overall length: 115 mm). Likewise, Ti-6Al-4 V was cut according to subsize specimen dimensions.

As shown in Figure 2, in-situ thermomechanical tests (simultaneous application of induction heating and static load) were conducted using EasyHeat 10 kW by Ambrell. After trial tests under different static loads and at various amperages, it is decided to conduct the experiments at 275 kHz, 300.3 A heating via a four-turn induction coil with an inner diameter of 40 mm and under a static load of 110 kg. During the experiments, temperature measurements at the bondline, on the CFRP overlap region and Ti-6Al-4 V surface (2–4 cm away from the bondline) were recorded using a FLIR A655sc long-wave infrared (LWIR) camera.

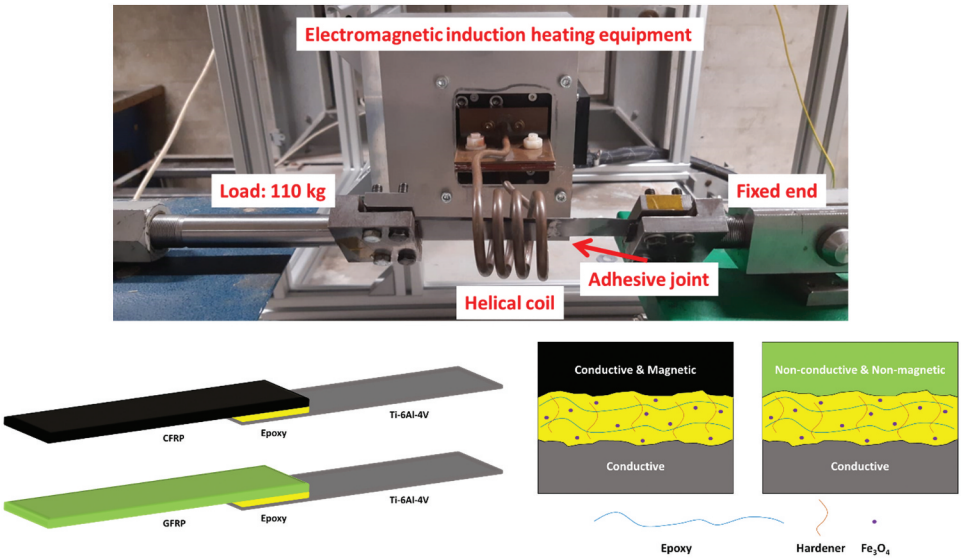

Figure 2. In-situ electromagnetic induction heating under a 110 kg load system (top) and schematic illustration of joint configurations.

3. Results and discussion

3.1. Thermal/Thermomechanical measurements

As Fe_3O_4 has an anisotropic shape and nonuniform distribution inside the epoxy, it is worth measuring CTE in different directions. The addition of Fe_3O_4 reduced CTE in the x- and y-directions of the epoxy, except for the 5 wt. % Fe_3O_4-epoxy in the y-direction (Table 5). On the other hand, the absolute value of CTE of epoxy in the z-direction (through-thickness) was increased by Fe_3O_4 addition except for 2 wt.% Fe_3O_4-epoxy (Figure 3a). More voids might be formed by the addition of particles which increases the viscosity of epoxy due to air entrapment. Thus, epoxy with high Fe_3O_4 content shrinks more during heating by filling the voids. Thermal mismatch seems weaker for CFRP joints than for GFRP as GFRP has a small expansion characteristic in the z-direction while all other materials are shrinking in the z-direction (Figure 3b). As CTE depends on the component phase and their interactions with each other, a strong interfacial bonding reduces the CTE substantially.[26] Increasing Fe_3O_4 contents caused a somewhat decreasing CTE of epoxy as Fe_3O_4 has a low CTE.[27]

T_g of neat epoxy increased in the range of 0.6–2.7% with the incorporation of Fe_3O_4 particles. T_g of cured epoxy is related to the segmental mobility of molecules[28] and the slight increase in T_g points out the relatively good interfacial interaction between epoxy and Fe_3O_4 particles restricting the movement of polymer chains. DMA analysis unveiled temperature-dependent storage modulus (E') and tan δ of all materials (Figures 4–5) as well as T_g of

Table 5. Thermal/Thermomechanical properties of the materials.

Material type	$CTE_{heat, x}$ (μm/m°C)	$CTE_{heat, y}$ (μm/m°C)	$CTE_{heat, z}$ (μm/m°C)	*E′*@40 *c* (GPa)	*E′*@100 *c* (GPa)	*E′*@120 *c* (GPa)	tan δ (peak)	α (mm^2/s)	Tg (°C)
GFRP	30.2 ± 11	65.9 ± 19	30	21.2 ± 1.61	22.2±.294	21.1±.556	.139 ±.01	0.25	134.8
CFRP	18.9 ± 4.1	74.6 ± 16	−67 ± 30	17.7 ± 1.85	16.4 ± 1.53	16.1 ± 1.31	.259 ± .01	0.587 ± 0.0	197.5 ± 0.3
Ti-6Al-4 V	27.7 ± 6.5	120 ± 20	−26 ± 25	76.1 ± 13.4	75.9 ± 12.5	75.5 ± 12.4	.0173 ± .09	5.12 ± 0.2	-
0 wt.% Fe3O4-epoxy	238 ± 24	193 ± 20	−339 ± 24	1.74 ± .324	.628 ± .098	.249 ± .031	.346 ± .01	0.106 ± 0.0	114.7
2 wt.% Fe3O4-epoxy	152 ± 17	145 ± 8.3	−122 ± 61	1.37 ± .265	.612 ± .128	.285 ± .092	.368 ± .01	0.127 ± 0.0	117.1 ± 0.1
5 wt.% Fe3O4-epoxy	136 ± 8.4	262 ± 11	−545 ± 192	1.16 ± .240	.707 ± .125	.339 ± .064	.372 ±.01	0.143 ± 0.0	115.4 ± 3.8
10 wt.% Fe3O4-epoxy	137 ± 27	139 ± 36	−634 ± 199	1.20± .375	.593 ± .125	.275 ± .049	.341 ± .01	0.131 ± 0.0	117.8 ± 0.5

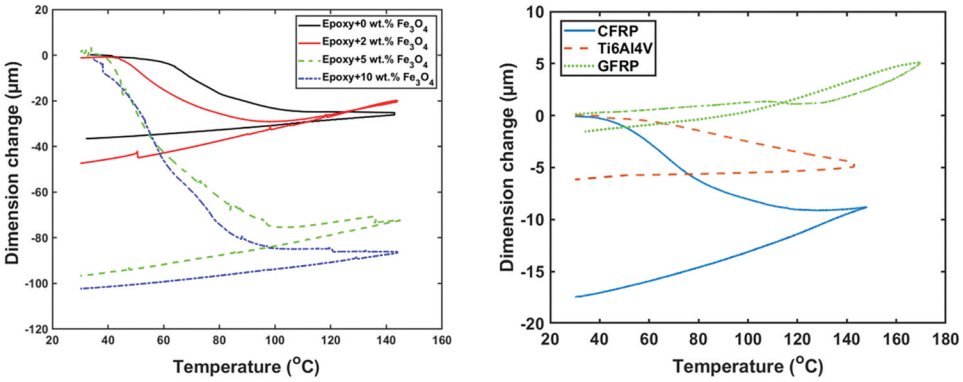

Figure 3. Effect of temperature on the z-direction dimension change of neat/hybrid epoxy samples and adherend materials.

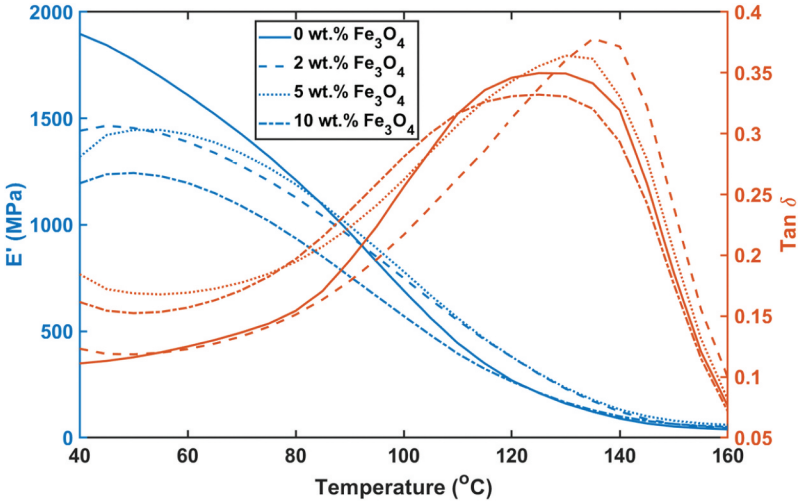

Figure 4. Effect of temperature on storage modulus (E') and tan δ of neat/hybrid epoxy laminates.

CFRP and GFRP. E' of neat epoxy was affected more than Fe_3O_4-epoxy samples with the increasing temperature. In other words, Fe_3O_4 enhanced the thermal stability of the epoxy, but it caused deterioration of the E' at room temperature conditions. Decreasing E' and increasing tan δ indicate a decrease in crosslinking by the addition of Fe_3O_4 particles.[29] T_g of GFRP and CFRP were found 134.8°C and 197.5°C, respectively. Measured T_g of CFRP was found very close to the nominal value of the technical data sheet (Table 3). At 120°C, E' of GFRP, CFRP, and Ti-6Al-4 V exhibited a reduction of 0.4%, 8.9%, and 0.8% respectively, compared to their respective values at room temperature. This decrease in storage modulus indicates a slight decrease in stiffness or rigidity of the materials at elevated temperatures. Although GFRP has lower T_g than CFRP, it has higher E' and a lowertan δ which can be

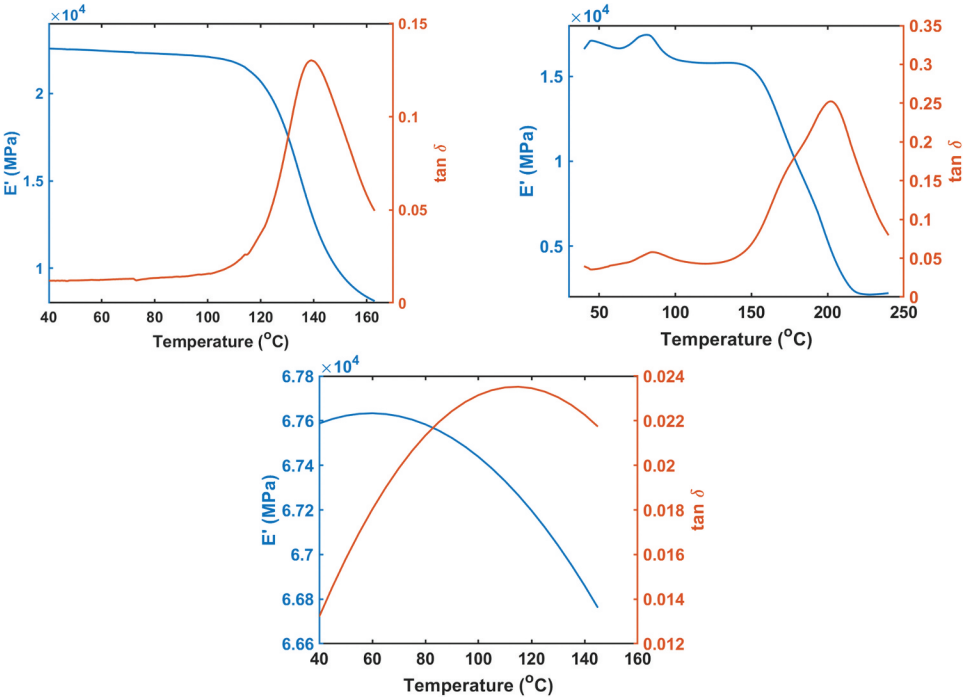

Figure 5. Effect of temperature on storage modulus (E′) and tan δ of GFRP (top left) CFRP (top right) and Ti-6Al-4V (bottom).

interpreted as a comparable adhesion between the resin and fibers for both materials at 120°C. Thermal diffusivity, α, of Ti-6Al-4 V (shown in Table 5) is the highest among all adherend materials while α of CFRP has almost one order of magnitude lower value than Ti-6Al-4 V. Thermal diffusivity of GFRP was half the value of CFRP. Neat epoxy has the lowest α while the addition of Fe_3O_4 increased α of all Fe_3O_4-epoxy a minimum of 15% because Fe_3O_4 has higher thermal diffusivity (proportionally higher thermal conductivity) than epoxy. Notably, 10 wt.% Fe_3O_4-epoxy has lower thermal diffusivity than 5 wt. % Fe_3O_4-epoxy due to the air entrapment in the epoxy + Fe_3O_4 mixture during mixing.[30] It is known that air has lower thermal conductivity than polymers. Therefore, high % of the air inside epoxy reduced the thermal diffusivity of the epoxy + Fe_3O_4 mixture.

3.2. Bulk material property characterization

The displacement of the deformation was measured using the crosshead movement during the uniaxial tensile testing. Room temperature and approximately 100°C tests were conducted on dogbone specimens of all materials using the digital image correlation (DIC) technique. In all specimens, the deformations were predominantly localized in the failure

region. The incorporation of Fe_3O_4 particles resulted in a reduction in the maximum strain to failure, indicating increased brittleness of the epoxy. Additionally, Fe_3O_4 particles caused a decrease in the elastic modulus and tensile strength of the epoxy at both room and elevated temperatures. This can be attributed to the spherical morphology (low aspect ratio) of the Fe_3O_4 particles[31] as well as the possible stress concentration caused by particle agglomeration.[32] The presence of any voids in the epoxy-Fe_3O_4 mixture may have further contributed to these effects. It is worth noting that neat epoxy samples were tested around 91.2°C while Fe_3O_4-epoxy were tested around 104°C. An increase in temperature led to increased strain to failure as all materials become more ductile at higher temperatures.

When CFRP was heated to a temperature of 111.5°C, significant mechanical degradation was observed. The elastic modulus and failure stress (σ_{fail}) of the CFRP were reduced by 63.9% and 60.6% respectively. This indicates a substantial decrease in the material's stiffness and load-bearing capacity under elevated temperature conditions. The room temperature properties of GFRP were obtained from the technical data sheet and in a comparative study.[20] GFRP at the elevated temperature had 44.1% lower elastic modulus and 44.8% lower σ_{fail} compared with the room temperature properties. Despite the average testing temperature of GFRP being 20.2°C lower than that of CFRP, the CFRP exhibited a higher elastic modulus at 111.5°C compared to GFRP. This suggests that CFRP retains its stiffness better at elevated temperatures compared to GFRP. However, it is important to note that the tensile strengths of GFRP were higher than those of CFRP at both temperatures as indicated in Tables 2 and 3. This indicates that GFRP possesses greater resistance to failure under both low and elevated temperature conditions compared to CFRP. As provided in Table 6, Ti-6Al-4 V has lower mechanical properties at an elevated temperature of 106°C (Fig. S1). Tensile yield, ultimate and failure stresses (σ_{Yield}, σ_{UTS} and σ_{fail}) decreased by 8.9%, 5.5% and 15.4% with increasing temperature, respectively, due to thermal softening and Elastic modulus decreased by 45.9%. Average ε_x and ε_y were changed by −27.5% and 24.7% at the failure point with about 80°C rise of temperature (from room temperature) which makes it more ductile (Fig. S2). Additionally, the average $\varepsilon_{y,yield}$ at room and elevated temperatures are 1.61% and 1.90% whilst average $\varepsilon_{y,UTS}$ are 12.5% and 13.7%, respectively. Consequently, it can be anticipated that there will be increased rotation, crack initiation, and propagation at the overlap end of Ti-6Al-4 V during the single lap joint (SLJ) tests at both temperatures. The strain mismatch between the epoxy and Ti-6Al-4 V is expected to amplify due to the thermal mismatch between the two materials. Ti-6Al-4 V exhibits a positive correlation with increasing temperature, while epoxy demonstrates a negative correlation. Moreover, incorporation of Fe_3O_4 into the epoxy further stiffens the adhesive. These factors contribute to the generation of thermal

stresses at the interface between the adhesive and the adherent, particularly near the adhesive-free ends and the adhesive-adherend interface.[33]

CDBC (i.e., tapered double cantilever beam TDCB) was employed to determine the adhesive fracture energy, G_{IC}, according to the simple beam theory (SBT) as:[34]

$$G_{IC} = \frac{4P^2}{Eb^2}\left(\frac{3a^2}{h^3} + \frac{1}{h}\right) \tag{1}$$

where P is the applied load, E is the aluminium Young's modulus (assumed as 69 MPa) and the geometry factor, h is the height of the aluminium adherend (19.4 mm) and a is the crack length (80 mm).

Adding Fe_3O_4 showed a toughening effect on the adhesive except for 5 wt.% Fe_3O_4 case that has a 3.9% lower *GIC*, than neat epoxy. On the other hand, 2 wt.% and 10 wt.% Fe_3O_4 loading have 39.0% and 37.0% higher G_{IC}, respectively. This can be interpreted as restricted crack propagation at the z direction (through-thickness) due to likely plastic void growth by inclusions of nanoparticles.[35] Although, other characterization results (mostly x and y directions) revealed adverse effects of Fe_3O_4 on the mechanical properties of epoxy. Table 6 lists that the average residue on the aluminium surface, measured through image processing of failure surfaces, increased with the incorporation of Fe_3O_4 particles. This indicates a shift towards a more cohesive type of failure, indicating improved adhesion of the hybrid epoxy to the adherend surface. Moreover, this increase in residue is associated with an enhancement in fracture toughness, specifically for the 2 wt.% and 10 wt.% Fe_3O_4 loadings. CTE of neat/hybrid epoxy samples affected somewhat their failure strain. For example, 2 wt.% Fe_3O_4 inclusion diminished the CTE of neat epoxy. Consequently, the difference between the strain values of neat epoxy at room and the elevated temperature was decreased after introducing 2 wt.% Fe_3O_4.

3.3. Surface roughness and contact angle analysis

The surface profiles of untreated and sandblasted CFRP, GFRP and Ti-6Al-4 V were characterized because the surface properties effect such as skewness and kurtosis the bonding and debonding behavior the joint.[36] The results are shown in Figures 6–8, respectively. After sandblasting, the fibers of FRP composites were exposed at the surface (CFRP-woven, GFRP-unidirectional) as sandblasting mainly results in the removal of the epoxy. Table 7 lists the surface roughness measurements of CFRP, GFRP and Ti-6Al-4 V. The difference between peaks and valleys for all materials was increased after the sandblasting. After sandblasting, the surface roughness of CFRP, GFRP and Ti-6Al-4 V increased by 1121%, 111% and 10.5%, respectively. Ra,1 of

Table 6. The mechanical properties of the bulk materials.

Material type	G_{IC} (kJ/m^2)	Average % of residues	Elastic modulus (GPa)	σ_{Yield} (MPa)	σ_{UTS} (MPa)	σ_{fail} (MPa)	ε_x (%)	ε_y (%)	Temp. (°C)
GFRP	-	-	46, 25.7 ± 2.1 25.7 ± 2.1	-	-	950, 524 ± 76 524 ± 76	-, −1.87 ± 0.27	-, 3.72 ± 0.14	23, 91.3 ± 9.2 91.3 ± 9.2
CFRP	-	-	73.9, 26.7 ± 3.0 26.7 ± 3.0	-	-	885, 349 ± 50 349 ± 50	-, −0.83 ± 0.48	-, 2.62 ± 0.47	23, 111.5 ± 4.2
Ti-6Al- 4V	-	-	88.0 ± .75 82.8 ± 5.3 82.8 ± 5.3	856 ± 20, 780 ± 15 780 ± 15	906 ± 20, 856 ± 14 856 ± 14	852 ± 10, 721 ± 18 721 ± 18	−11.6 ± 2.7, −14.8 ± 1.4	29.2 ± 4.3, 36.4 ± 4.7	23, 106.0 ± 1.2 106.0 ± 1.2
0 wt.% Fe3O4-epoxy epoxy	1.54 ± 0.11	68.5 ± 4.1	1.72 ± .41, .517 ± .02 0.517 ± 0.02	-	-	25.4 ± 1.0, 1.41 ± .2 1.41 ± 0.2	−4.67 ± 0.47, −4.33 ± 0.47	13.9 ± 2.4, 16.2 ± 2.0	23, 91.2 ± 4.8 91.2 ± 4.8
2 wt.% Fe3O4-epoxy epoxy	2.14 ± 0.42	71.6 ± 5.4	1.62 ± .14, .479 ± .05 0.479 ± 0.05	-	-	22.6 ± 1.4, .93 ± .1 0.93 ± 0.1	−3.08 ± 2.3, −4.66 ± 0.12	10.7 ± 3.2, 10.2 ± 0.94	23, 104.3 ± 6.1 104.3 ± 6.1
5 wt.% Fe3O4-epoxy epoxy	1.48 ± 0.24	68.8 ± 2.9	1.52 ± .11, .239 ± .09 0.239 ± 0.09	-	-	23.5 ± 1.0, .82 ± .1 0.82 ± 0.1	−2.58 ± 1.3, −3.50 ± 1.0	7.87 ± 2.6, 15.7 ± 0.05	23, 103.4 ± 6.1 103.4 ± 6.1
10 wt.% Fe3O4-epoxy epoxy	2.11 ± 0.36	89.2 ± 9.4	1.54 ± .10, .311 ± .04 0.311 ± 0.04	-	-	21.6 ± .7, .91 ± .3 0.91 ± 0.3	−3.55 ± 1.5, −2.98 ± 0.34	7.88 ± 2.8, 9.99 ± 0.15	23, 104.3 ± 3.1 104.3 ± 3.1

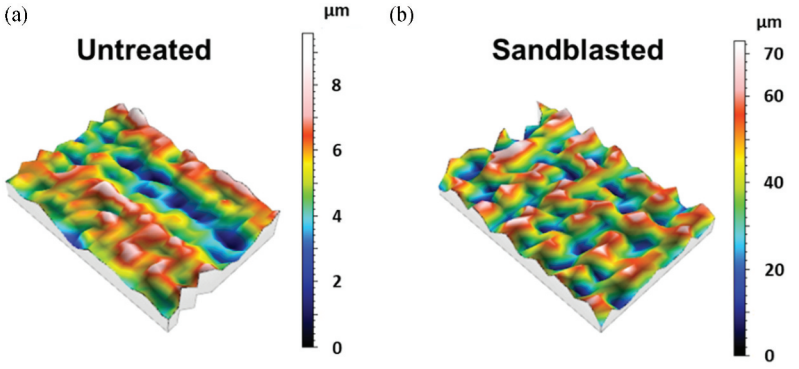

Figure 6. The surface profile of (a) untreated and (b) sandblasted CFRP adherends.

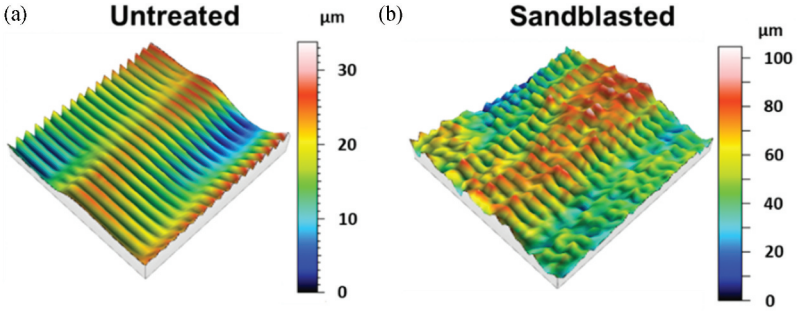

Figure 7. The surface profile of (a) untreated and (b) sandblasted GFRP adherends.

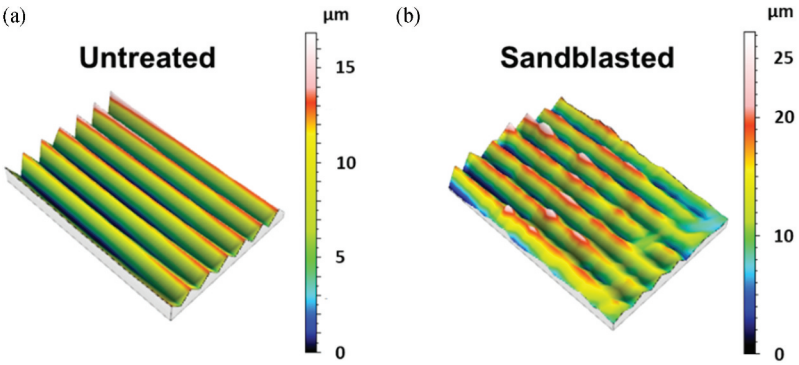

Figure 8. The surface profile of (a) untreated and (b) sandblasted Ti-6Al-4V adherends.

untreated CFRP, GFRP and Ti-6Al-4 V increased by 1232%, 111% and 10.4%, whereas Ra,2 of untreated CFRP, GFRP and Ti-6Al-4 V enhanced by 2585%, 1840% and 927% after sandblasting, respectively. Sssk of the CFRP is lower than 0 and hence its surface has valleys before and after sandblasting mostly. The surfaces of GFRP (only sandblasted) and Ti-6Al-4 V have positive S_{ssk}

Table 7. Three and two-dimensional surface roughness parameters.

Adherend type	S_a (μm)	S_q (μm)	S_{ssk}	S_{ku}	S_p (μm)	S_v (μm)	S_z (μm)	$*R_{a,1}$ (μm)	$*R_{a,2}$ (μm)
Untreated CFRP	1.12	1.40	−0.18	3.11	3.76	4.12	7.89	0.56	0.27
Sandblasted CFRP	13.7	16.0	−0.04	2.07	38.3	36.9	75.1	7.46	7.25
Untreated GFRP	6.29	8.29	−0.52	9.34	36.2	47.7	83.8	4.09	0.20
Sandblasted GFRP	13.3	16.6	0.27	3.06	58.5	46.6	105	11.1	3.88
Untreated Ti-6Al-4V	4.96	5.14	0.22	1.92	8.64	7.17	15.8	4.90	0.11
Sandblasted Ti-6Al-4V	5.48	6.21	0.30	2.63	22.1	13.3	35.4	5.41	1.13

$*R_{a,1}$ and $*R_{a,2}$ -→ Gaussian filter, 0.8 mm.

Table 8. The water contact angle of CFRP and Ti-6Al-4 V.

Adherend type	Contact angle in degrees
Untreated CFRP	80.9 ± 2.7
Sandblasted CFRP	79.2 ± 3.4
Untreated GFRP	73.1
Sandblasted GFRP	57.3
Untreated Ti-6Al-4V	61.6 ± 5.4
Sandblasted Ti-6Al-4V	82.7 ± 6.5

values which indicate peaks are more than valleys before and after sandblasting. Sandblasting resulted in lowering S_{ku} for untreated CFRP, GFRP and Ti-6Al-4 V surfaces which is an indication of removing surface defects of untreated samples.

Sandblasting of untreated CFRP led to a minor change (2.1%) in the water contact angle as indicated in Table 8. Interestingly, sandblasting of Ti-6Al-4 V increased the water contact angle despite the similar enhancement in surface roughness as reported in.[37] This phenomenon could be attributed to the potential alteration of the chemical composition on the surface, such as a decrease in titanium (Ti) content and an increase in aluminium (Al) content, caused by the aluminium oxide grid-blasting process. Similar findings have been reported by Costa et al..[38] The rise in water angle indicates a decrease in the wettability of Ti-6Al-4 V surfaces and the increased likelihood of air entrapment at the surface.

3.4. Single lap joint (SLJ) tests

The effects of different wt.% of Fe_3O_4 on the SLJ were investigated at room temperature conditions. The lap shear strength versus displacement response curves depicted in Figure 9 shows an initial linear response up to around 0.5 mm followed by non-linear response similar to that of is typical for dissimilar joints.[14] The DIC technique was utilized to understand full-field strain distribution on the SLJ samples using three different cameras simultaneously. Strain distribution in the x, y (transverse and longitudinal directions, respectively) and major axes are shown in Figures 12–13. The x, y and major axes strains were more dominant at the overlap ends of the joints than the middle

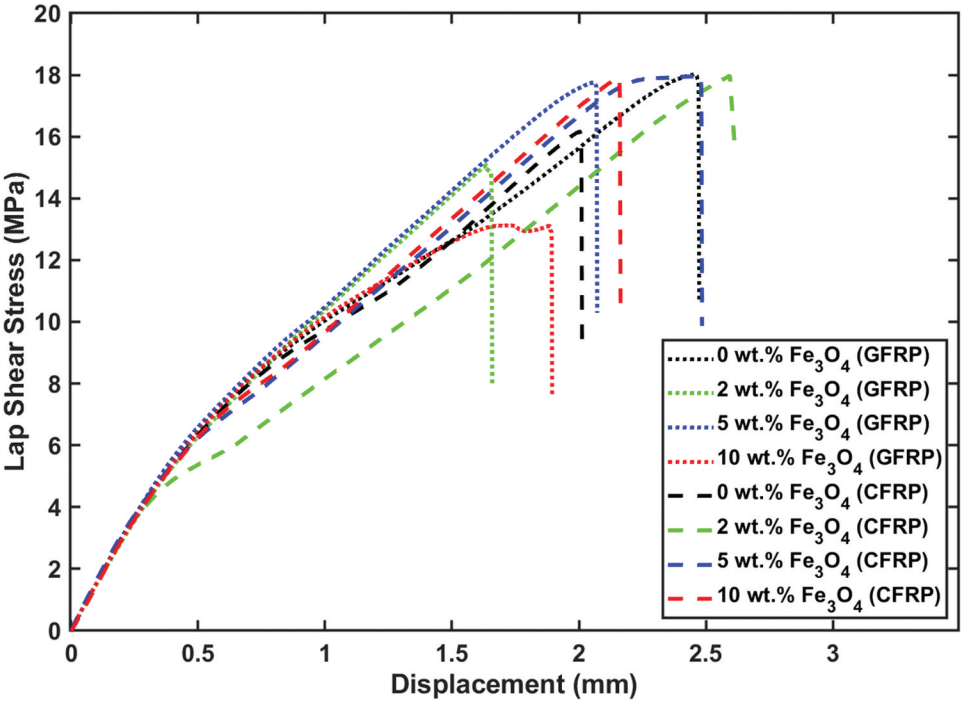

Figure 9. Representative lap shear stress cross-displacement responses of the joints.

region. The strain distribution on the major axis is computed by GOM software using the principal axis transformation of the strain tensor.[39, 40] The strain distributions along the major axis and x-axis exhibit similarities, suggesting that peel stresses are predominant. Additionally, the maximum strain along the major axis occurs at the ends of the overlap regions. The bondline ends undergo significant deformation due to bending, particularly after the non-linear deformation caused by increasing load eccentricity. As indicated in Table 9, CFRP-Ti-6Al-4 V joints exhibited superior SLJ than GFRP/Ti-6Al-4 V joints, primarily due to CFRP has a higher elastic modulus than GFRP. Despite GFRP having better wettability characteristics, the lower elastic modulus of GFRP resulted in reduced joint strength. Additionally, CTE mismatch is higher for GFRP/Ti-6Al-4 V which causes thermally induced stresses (during the curing process) and/or the anisotropic nature of GFRP may have led to strength reduction.[37] Although adding Fe_3O_4 to epoxy did not always increase the SLJ strength of the joints, the % epoxy residue always higher on the Ti-6Al-4 V surfaces compared with the neat epoxy joints as shown in Figures 10–11. The difference between trends might result from a CTE mismatch between the Fe_3O_4-epoxy and the adherends due to high temperature curing. Neat (0%) epoxy configuration of GFRP/Ti-6Al-4 V joints induced lower SLJ at room temperature conditions than GFRP/GFRP joints, as reported in our previous study[22] because of a lower bending stiffness of Ti-

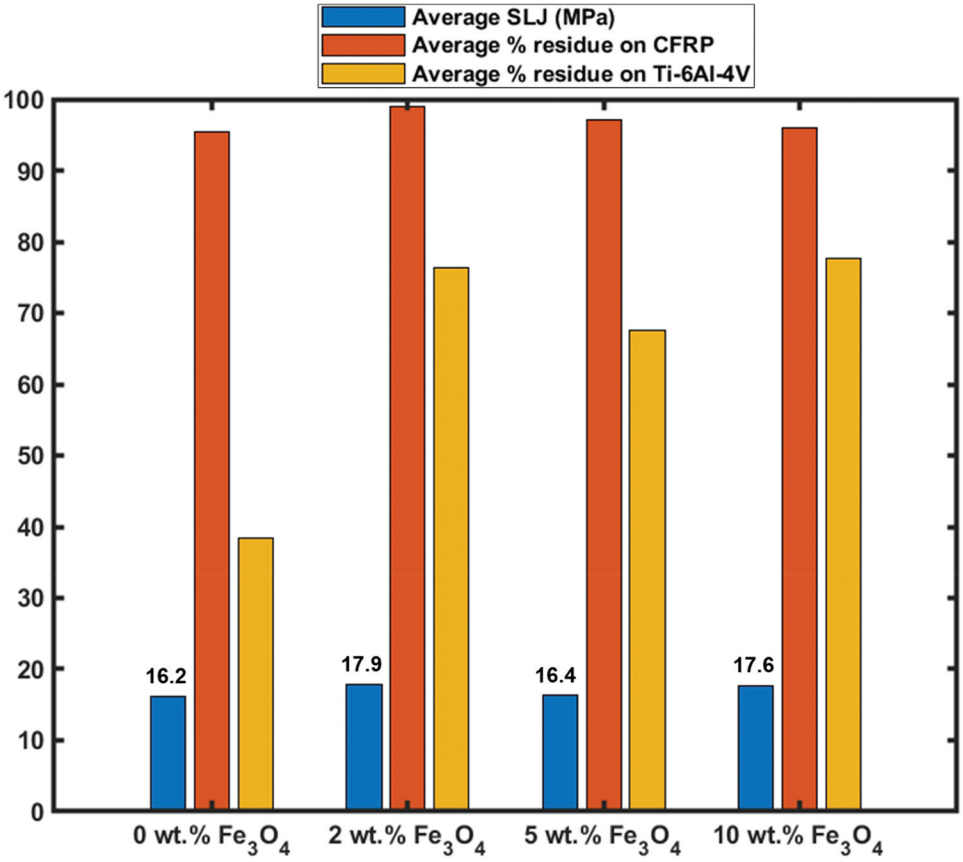

Figure 10. The results of the SLJ test conducted on CFRP/Ti-6Al-4V joints.

6Al-4 V (0.5 mm thick) than GFRP (2.5 mm thick).[41] Besides, thin metal adherends are prone to experiencing plastic deformation, leading high localized strains might reduce SLJ strength.[42] CFRP does not display yielding under tension as it is an elastic-brittle material.[43] The joints between CFRP and Ti alloy, which were bonded using epoxy adhesive reinforced with 5 wt.% nanoparticles, exhibited a mixed failure mode along with lower strength when compared to joints reinforced with 2 and 10 wt.% nanoparticles. Conversely, the other mixtures resulted in cohesive failure. Table 6 indicates that the fracture toughness was lower for the 5 wt.% joints, making them unable to withstand relatively high peel stresses. Consequently, the 5 wt.% joints failed at a lower load compared to the 2 and 10 wt.% joints. Figures 12 and 13 provide visual evidence of the different deformation behaviours of the materials after failure. In the case of Ti-6Al-4 V, plastic deformation is observed, indicated by the permanent change in shape even after the failure event. The Ti-6Al-4 V side of the joint exhibits higher deformation compared to CFRP and GFRP depicting asymmetrical deformation due to mismatch in material properties and free-edge stress concentration factors. The higher deformation in the Ti-

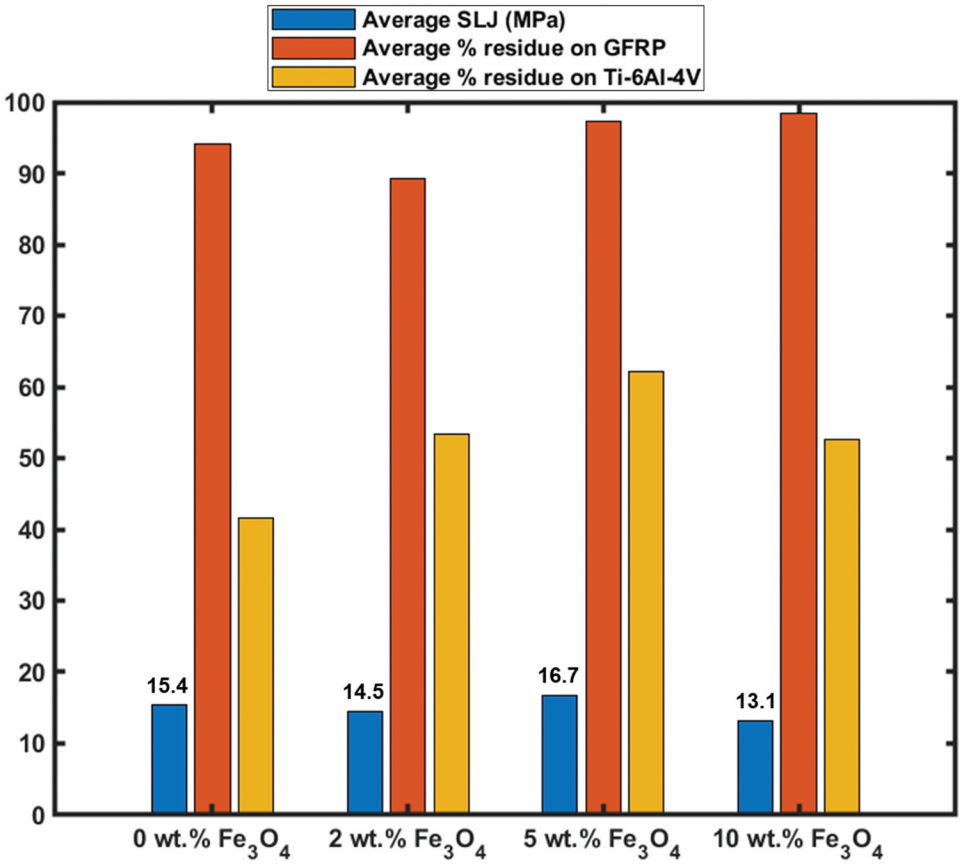

Figure 11. The results of the SLJ test conducted on GFRP/Ti-6Al-4V joints.

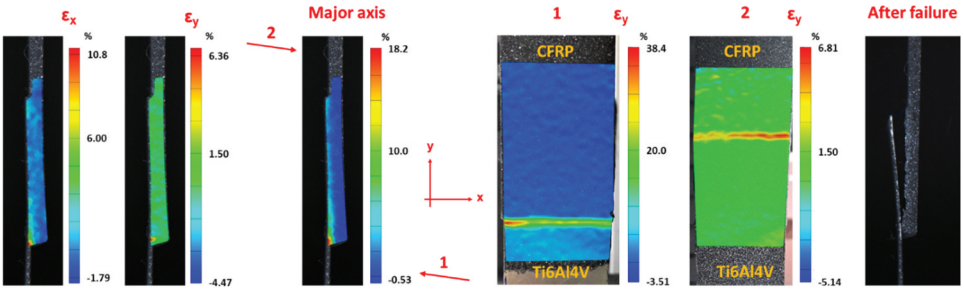

Figure 12. Strain distribution for 2 wt.% Fe_3O_4-Epoxy (CFRP/ti-6Al-4V) joint and after failure.

6Al-4 V side may lead to localized stress concentrations and can contribute to crack initiation. The strains observed near the lap ends are commonly associated with the formation of a hinge-like behaviour, where compressive strains develop.[14] This hinge formation can result from the non-linear deformation of the joint under load, leading to concentrated stresses near the lap ends. The remaining areas experienced almost zero strain i.e., small deformations

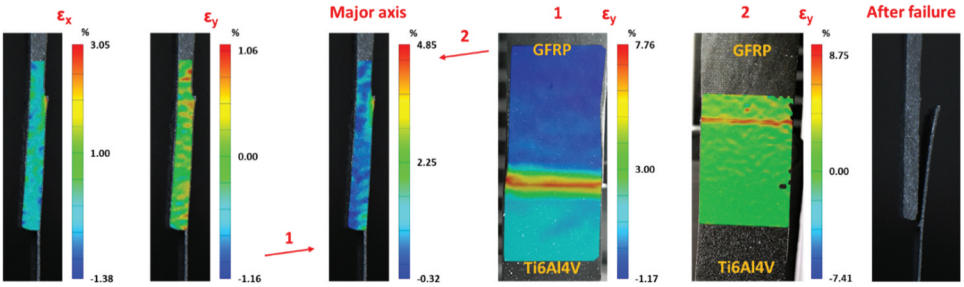

Figure 13. Strain distribution for 5 wt.% Fe_3O_4-Epoxy (GFRP/ti-6Al-4V) joint and after failure.

existence. Ti-6Al-4 V was fixed from the end while the samples were pulled from the composite adherends' side during the tests. The strains at the lap end of composite adherends were found higher than Ti-6Al-4 V. It is known that crack initiation happens at the bondline of similar joints symmetrically. However, as dissimilar joints were investigated here, cracks initiate at one of the overlap ends randomly (Figures 12–13). The rotation angle was correlated with the SLJ strength mostly. In general, the high displacement induced a higher rotation angle and CFRP had a higher rotation angle than GFRP due to being thinner and hence less stiff but having a higher strength than GFRP joints. Additionally, the strain distribution in the y-direction is higher at the inner surfaces of the adherends (bonded side) compared to the outer surfaces, as shown in Figures 12–13 where #1 and #2 correspond the cameras' viewing from either left or right of the joint. #1 shows the inner (bonded) surface of Ti-6Al-4 V and outer surfaces of FRP adherend whilst #2 shows the inner (bonded) surface of FRP adherend and outer surface of Ti-6Al-4 V. This observation indicates that the highest strains and deformations occur in the region where the adhesive interacts with the adherends, suggesting the presence of localized stress concentration in the bonded area. Especially Ti-6Al-4 V demonstrated higher strain in the inner surfaces (#1) which were higher strain than FRP adherends. In other words, nonuniform through-thickness strain and displacement distributions.

Better wettability of GFRP and CFRP promoted a higher % of epoxy residue on their surfaces than Ti-6Al-4 V. The % residue correlated with S_a of the material surfaces positively. CFRP surfaces had slightly more epoxy residue compared to GFRP surfaces due to lower S_{ku} of CFRP minimizes the stress concentrations at the surface and allows for better adhesion between the epoxy and CFRP.[36] On the other hand, the low yield strength of Ti-6Al-4 V may contribute to interfacial failure,[44] resulting in a lower amount of residue. Also, Ti-6Al-4 V exhibited the poor wettability characteristics (lowest surface roughness and highest contact angle after sandblasting) among the three adherend types which contributed to the low epoxy residue. Still, almost all joints displayed a mixed failure mode. The cohesive failure mode only

Table 9. Lap shear test measurements.

Adherend type	Material type	Average SLJ (MPa)	Average displacement (mm)	Average rotation angle (°)	Average % of residues (on GFRP or CFRP)	Average % of residues (on Ti-6Al-4 V)	Failure mode
CFRP/Ti-6Al-4 V	0 wt.% Fe3O4-epoxy	16.2 ± 0.9	2.20 ± 0.47	3.24	95.4	38.4	M
	2 wt.% Fe3O4-epoxy	17.9 ± 2.4	3.27 ± 0.10	3.08	98.9	76.4	C
	5 wt.% Fe3O4-epoxy	16.4 ± 0.1	2.39 ± 0.30	2.42	97.1	67.5	M
	10 wt.% Fe3O4-epoxy	17.6 ± 2.5	2.54 ± 0.40	2.33	95.9	77.6	C
GFRP/Ti-6Al-4 V	0 wt.% Fe3O4-epoxy	15.4 ± 1.7	2.12 ± 0.31	2.64	94.1	41.5	M
	2 wt.% Fe3O4-epoxy	14.5 ± 0.1	2.20 ± 0.41	1.63	89.2	53.4	M
	5 wt.% Fe3O4-epoxy	16.7 ± 0.5	2.13 ± 0.19	3.08	97.2	62.1	M
	10 wt.% Fe3O4-epoxy	13.1 ± 0.5	1.73 ± 0.18	1.66	98.5	52.7	M

A: Adhesive, C: Cohesive, M: Mixed. $100 \leq A \leq 133 < M \leq 167 < C \leq 200$.

appeared at the two highest strength CFRP joints. Light fiber tearing on GFRP surfaces was found but almost none for CFRP even if SLJ for CFRP joints were higher. The findings from our study, supported by reference[41] and illustrated in Fig. S3, confirm that woven composites, specifically CFRP in this case, exhibit a lower susceptibility to delamination. This characteristic is attributed to the inherent structural properties and interlocking nature of the woven fabric reinforcement, which enhances the interlaminar strength and resistance to separation between layers. Contrarily, GFRP adherends indicated delamination as shown in Fig. S4. Shear bands were formed at the bondline of 5 wt.% Fe_3O_4 GFRP joint and 2 wt.% Fe_3O_4 CFRP joint as an indication of the enhancement of shear strength of the joints. The epoxy residue was smooth on the CFRP and GFRP surfaces mainly as this displayed the high peel stresses while Ti-6Al-4 V presented rough epoxy residue which pointed out shear stress was predominant. The incorporation of Fe_3O_4 led to by 26% to 99% increase in the adhesive residue that indicates an enhancement of the adhesion between epoxy and Ti-6Al-4 V surface. Although additional of Fe_3O_4 decreased the storage modulus of epoxy, Fe_3O_4 increases the lap shear strength in most cases due to its better wettability. Compared with neat epoxy GFRP/GFRP joints,[22] GFRP/Ti-6Al-4 V joints had more epoxy residue on their surfaces.

3.5. In-situ electromagnetic induction heating under a static loading

In this study, dissimilar joints, specifically CFRP/Ti-6Al-4 V joints and GFRP/Ti-6Al-4 V joints with GFRP adherends of different thicknesses (around 2.60 mm for thin and around 3.30 mm for thick), were subjected to in-situ electromagnetic induction heating under a constant static loading of 1.1 kN. The joints were modified with different weight percentages of Fe_3O_4-epoxy. The purpose of the experiment was to investigate the effects of in-situ heating and Fe_3O_4-epoxy content on the joint's mechanical behavior. The geometrical details of the dissimilar joints were tabulated in Table 10. The bondline thicknesses at the end of CFRP were 2–3 times thicker than Ti-6Al-4 V which probably resulted from insufficient molding. However, the same molding technique provided more uniform bondline thickness along the overlap. The size of the overlap area was similar among all joints. 2 wt.%. Fe_3O_4-epoxy bonded CFRP/Ti-6Al-4 V joints had a lightly thicker bondline at the free end of the CFRP side and a thinner bondline at the free end of the Ti-6Al-4 V side as indicated in Table 10.

The thermal images of some tests just after failure are shown in Figure 14. The joint overlap region was located between the first and third coils from the left. As the content of Fe_3O_4within epoxy increases, the temperature distribution in the overlap region of Ti-6Al-4V just after failure became more uniform. More than the overlap region of all adherends were sandblasted before the

Table 10. Geometrical details of in-situ heated joints.

Adherend materials	wt. % of Fe_3O_4 particles	Average thickness of Adh-1 (mm)	Average bondline thickness at end of Adh-1 (mm)	Average thickness of Adh-2 (mm)	Average bondline thickness at end of Adh-2 (mm)	Average overlap length (mm)	Average overlap width (mm)
CFRP/Ti-6Al-4V	0	2.21 ± 0.06	0.35 ± 0.04	0.48 ± 0	0.14 ± 0.05	24.8 ± 0.1	25.5 ± 0.0
	2	2.23 ± 0.01	0.37 ± 0.06	0.45 ± 0	0.14 ± 0.04	25.2 ± 0.1	25.3 ± 0.0
	5	2.20 ± 0.01	0.27 ± 0.10	0.50 ± 0.02	0.11 ± 0.04	25.4 ± 0.1	25.4 ± 0.0
	10	2.20 ± 0.02	0.36 ± 0.04	0.47 ± 0.02	0.14 ± 0.05	25.5 ± 0.0	25.4 ± 0.1
GFRP (thin)/Ti-6Al-4V	0	2.50 ± 0.03	0.17 ± 0.03	0.50 ± 0.01	0.24 ± 0.12	25.1 ± 0.0	23.9 ± 0.2
	2	2.56 ± 0.02	0.25 ± 0.07	0.49 ± 0.02	0.22 ± 0.07	25.5 ± 0.0	25.0 ± 0.0
	5	2.72 ± 0.13	0.19 ± 0.11	0.48 ± 0	0.23 ± 0.13	25.2 ± 0.0	24.5 ± 0.0
	10	2.70 ± 0.22	0.24 ± 0.11	0.51 ± 0.01	0.19 ± 0.08	24.9 ± 0.0	24.9 ± 0.1
GFRP (thick)/Ti-6Al-4V	2	3.29 ± 0.01	0.09 ± 0.01	0.49 ± 0	0.11 ± 0.01	25.4 ± 0.0	24.5 ± 0.1
	5	3.29 ± 0.13	0.18 ± 0.07	0.48 ± 0	0.20 ± 0.06	25.4 ± 0.0	24.4 ± 0.1
	10	3.38 ± 0.05	0.14 ± 0.06	0.48 ± 0.01	0.19 ± 0.07	25.1 ± 0.0	24.5 ± 0.2

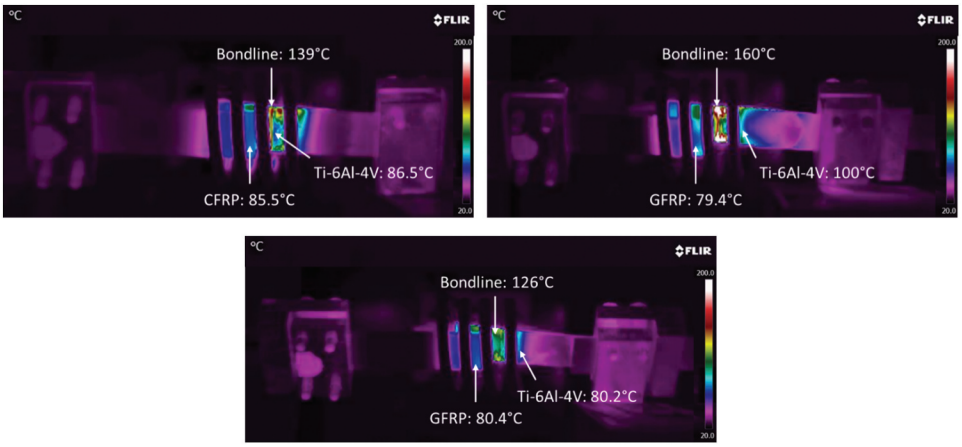

Figure 14. Thermal images of 2 wt.% Fe_3O_4 epoxy bonded CFRP/Ti-6Al-4V joint (top left), 5 wt.% Fe_3O_4 epoxy bonded GFRP (thin)/Ti-6Al-4V joint (top right) and 5 wt.% Fe_3O_4 epoxy bonded GFRP (thick)/Ti-6Al-4V joint (bottom).

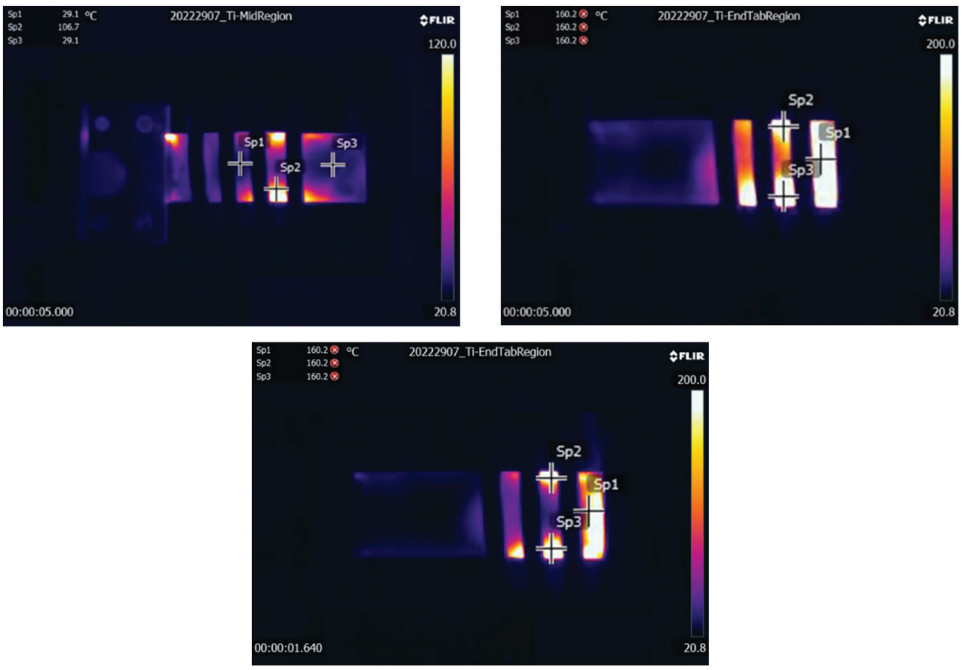

Figure 15. Thermal image of Ti-6Al-4V (untreated (top left) & sandblasted sample (top right)) at 5th second of the test and sandblasted at 1.6th second (bottom).

tests. Remarkably, an interesting observation was made during the induction heating process: the sandblasted regions of Ti-6Al-4V heated up faster than the untreated region (as depicted in Figure 15). This can be attributed to the surface cleaning effect of sandblasting on Ti-6Al-4V, which eliminates surface contaminants that can hinder efficient heating through a shielding effect.[45]

Additionally, the sandblasting process can alter the electrical conductivity of the surface, enhancing its Joule heating capability and further contributing to the accelerated heating of the sandblasted regions. Similarly, sandblasting can activate the Ti-6Al-4V surface by creating micro-roughness and introducing surface irregularities. These activated surfaces can exhibit improved receptivity to electromagnetic energy, promoting more effective heat generation during induction heating. As shown in Figure 15 (bottom), reaching the maximum readable temperature (160.2°C) of the thermal camera at Sp1, Sp2 and Sp3 points on the sandblasted surface of Ti-6Al-4V took 0.80 s, 1.64 s and 1.00 s, respectively. On the other hand, electromagnetic induction heating of untreated and sandblasted GFRP was unsuccessful to heat up by electromagnetic induction as GFRP does not carry electrical/magnetic properties. In Tables 10–11, the geometrical dimensions and temperature profile with time to failure of tested joints are listed, respectively. As demonstrated in Figure 17, CFRP joints with pure epoxy exhibited a shorter time to failure compared to GFRP joints as CFRP has an induction heating capability as it is electrically conductive and exhibits relative magnetism.[46] In contrast, thicker GFRP joints required a significantly longer time to fail, exceeding the failure time of thinner joints by more than 50%, as shown in Figure 16. The thicker adherends act as a thermal insulator, impeding the penetration of electromagnetic fields and reducing heat generation within the joint. The addition of Fe_3O_4 into the epoxy adhesive further reduced the time to failure.[16] This could be attributed to factors, such as enhanced electromagnetic coupling between the CFRP or Ti-6Al-4V adherends and the adhesive, improved heat generation within the joint, or altered mechanical properties of the adhesive itself. However, it is known that heat generation through magnetic hysteresis is generally much lower compared to heat generation through eddy currents.[45] Thus, when using 10 wt.% Fe_3O_4 epoxy bonded GFRP/GFRP joints, the electromagnetic induction heating is much slower than in GFRP/Ti-6Al-4V joints. Also, CFRP has higher electrical conductivity due to the higher carbon

Table 11. In-situ heated static test results.

Adherend materials	wt. % of Fe3O4 particles	Average Adh-1 Temp. (°C)	Average Adh-2 Temp. (°C)	Average Bondline Temp. (°C)	Average time to failure (s)	Failure mode
CFRP/Ti-6Al-4V	0	91 ± 4	65 ± 14	129 ± 6	33.6 ± 2.4	A
	2	101 ± 36	83 ± 19	131 ± 16	23.1 ± 5.2	A
	5	87 ± 7	83 ± 17	138 ± 15	31.2 ± 0.9	A
	10	91 ± 13	64 ± 6	128 ± 7	37.1 ± 12	A
GFRP (thin)/Ti-6Al-4V	0	91 ± 4	76 ± 14	126 ± 4	52.6 ± 5.4	A
	2	85 ± 3	76 ± 36	120 ± 10	46.7 ± 4.9	A
	5	72 ± 8	86 ± 36	139 ± 15	33.1 ± 5.6	A
	10	68 ± 9	65 ± 17	131 ± 6	30.4 ± 4.4	A
GFRP (thick)/Ti-6Al-4V	2	97 ± 12	62 ± 4	126 ± 13	70.4 ± 10	A
	5	77 ± 1	79 ± 8	116 ± 3	53.3 ± 2.8	A
	10	87 ± 7	79 ± 25	131 ± 15	65.0 ± 10	A

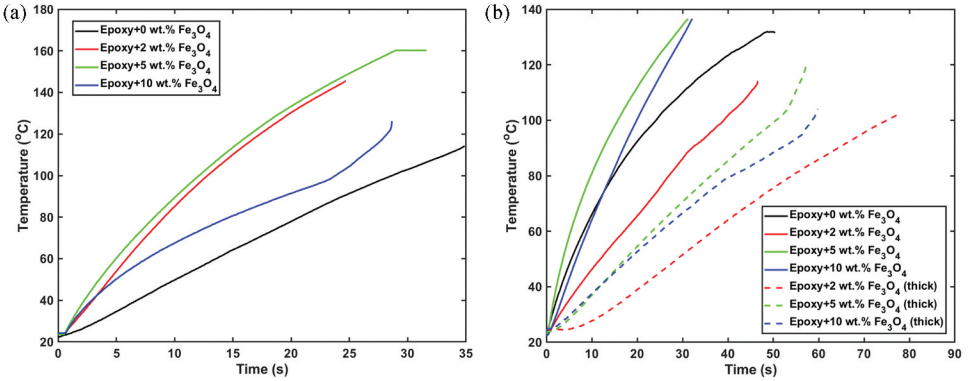

Figure 16. Representative temperature distribution at the bondline of (a) CFRP/Ti-6Al-4V joints and (b) GFRP/Ti-6Al-4V joints.

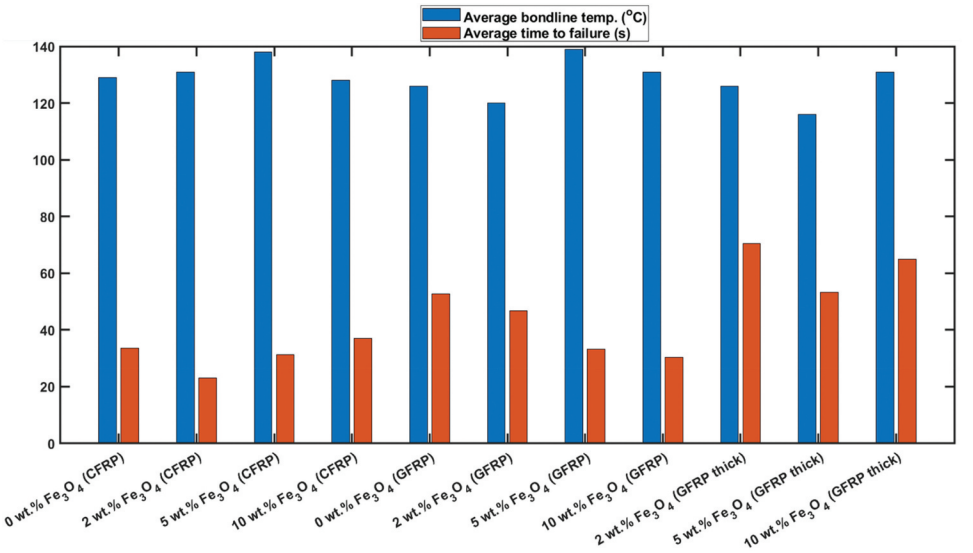

Figure 17. A brief summary of the results obtained from in-situ electromagnetic induction heating applied to CFRP/Ti-6Al-4V joints and GFRP/Ti-6Al-4V joints under static loading conditions.

content in CFRP compared to GFRP, which increases the Joule heating capability.[46] In general, GFRP samples with 5 wt.% iron oxide showed better debondability characteristics, requiring approximately 5% shorter time to fail, than samples with 10 wt.%. It should be noted that a thicker adhesive bondline may lead to better induction heating capabilities (i.e., faster heating) due to having more particles in the adhesive bondline. Among the CFRP-Ti joints reinforced with Fe_3O_4, those containing 2 wt.% and 5 wt.% exhibited comparable heating characteristics, while the joints with 10 wt.% Fe_3O_4 demonstrated inferior heating performance. This decrease in heating efficiency in the 10 wt.

% group could be attributed to factors such as particle agglomeration, voids, impeding the Joule heating by magnetic hysteresis. The addition of Fe_3O_4 particles to GFRP joints improved their heating capability by increasing their thermal conductivity. This was evident in the faster heating rates of GFRP joints reinforced with 5 wt.% and 10 wt.% Fe_3O_4, even though the GFRP adherends were 8% thicker compared to the joints reinforced with 0 wt.% and 2 wt.% Fe_3O_4 -epoxy. The higher concentrations of Fe_3O_4 (5 wt.% and 10 wt.%) likely exceeded the percolation threshold, enabling the formation of conductive pathways throughout the joint. These pathways facilitated efficient heat transfer, compensating for the increased thickness of the GFRP adherends. Consequently, the improved thermal conductivity and the presence of conductive pathways allowed for better distribution and dissipation of heat within the joint. For all joints, the 5 wt.% Fe_3O_4-epoxy in each group showed the best heating capability. Both joint configurations showed a decreasing heating rate with increasing temperature due to decreased magnetic properties of Fe_3O_4 at higher temperatures.[47] Secondly, although there may be a slight enhancement of the eddy current properties at elevated temperatures, the overall effect is limited. Additionally, the electrical resistivity of titanium alloy tends to increase with temperature,[48] further impeding the flow of electrical current and reducing the heating rate. In general, epoxy with Fe_3O_4 particles responds quicker as indicated in Figure 14, due to enhanced thermal diffusivity as indicated in Table 5.

Commonly, the epoxy residue on the Ti-6Al-4 V surface remained only at the end of overlap regions that point out the high peel stresses at those regions due to thermomechanical mismatches (Fig. S5-7). Another reason could be quickly heating Ti-6Al-4 V surfaces made the interface weaker compared to FRP-adhesive interfaces. Besides, thick GFRP joints had more epoxy residue (thin layer of epoxy) on thick GFRP joint surfaces. Generally, 10 wt.% joints had more epoxy residue left on Ti-6Al-4 V surfaces due to particles acting as stress concentrations inside the adhesive. Relatively, the epoxy residue was found more on CFRP than on GFRP. Smooth fracture surfaces without shear bands indicate the low shear strength of joints at elevated temperatures. Commonly, it was observed that an increase in the adherend temperature generated a lower % adhesive residue at the adherend surface.

4. Conclusions

The significance of Fe_3O_4 particles on the functionalization of epoxy adhesively bonded dissimilar joints was examined in this study. Fe_3O_4 enhanced the tensile fracture toughness of epoxy for 2 wt.% and 10 wt.% Fe_3O_4-epoxy. By the DIC technique, the tensile properties and CTE differences between different wt.% epoxy and adherend materials were established to understand the mechanical response of materials under thermomechanical load.

Sandblasting increased the surface roughness of the adherends substantially. However, contact angle analysis showed only enhancement in the wettability of GFRP surfaces after sandblasting. Surface roughness and water contact angle analysis helped to understand the failure mode of the SLJ samples and the residue epoxy on the adherend surfaces. Room temperature SLJ tests pointed out no substantial difference arising from adding Fe_3O_4 into the epoxy adhesive. Besides, Fe_3O_4 particles helped the debonding process of the joints by reducing the time of failure (i.e., less energy required). CFRP joints had a lower time of failure than GFRP joints as they have magnetic and electrical conductivity properties. Thicker GFRP adherends required a longer time for failure since GFRP does not have any magnetic/electrical capabilities. The electromagnetic induction trial of GFRP/GFRP joints was unsuccessful in terms of heating the samples to fail under a static load. Sandblasting had a significant impact on enhancing the induction heating capability of the Ti-6Al-4 V. To understand the underlying mechanism, further investigations are recommended. The future work may include electromagnetic induction curing of dissimilar joints with Fe_3O_4, chemical functionalisatoion of Fe_3O_4 particles for their dispersion to improve the effectiveness of magnetic hysteresis, joints with thicker titanium alloy because it has very limited penetration depth (less than 0.80 mm) at 275 kHz[48] and development of in-situ magentic heating system with peel or shear lap testing system.

Acknowledgement

CH thanks Nanyang Technological University for the financial support in the form a SINGA graduate scholarship. IS thanks National Research Foundation Singapore for financial support via Grant Number CRP29-2022-0041.

Disclosure statement

No potential conflict of interest was reported by the author(s).

Funding

This work was supported by the National Research Foundation [CRP29-2022-0041].

Nomenclature

A	adhesive failure
Al	aluminum
BET	Brunauer – Emmett–Teller
CDCB	contoured double-cantilever beam
CTE	coefficient of thermal expansion
DMA	dynamic mechanical analyzer

E	Young's modulus
EoLV	end-of-life vehicles
ε_y	failure strain in the y direction
FRP	fiber reinforced polymers
GIC	adhesive fracture energy
M	mixed failure
$R_{a,1}$	arithmetic mean height in the axial direction
S_a	arithmetic mean height
S_p	maximum height of peaks
S_{ssk}	skewness
S_z	maximum height of the surface
SLJ	single lap joint
σ_{UTS}	Ultimate tensile strength
tan δ	tan delta
T_g	glass transition temperature
GIC	thermal diffusivity
Al_2O_3	aluminum oxide
C	cohesive failure
CFRP	carbon fiber reinforced polymers
DIC	digital image correlation
DSC	differential scanning calorimetry
E′	storage modulus
ε_x	failure strain in the x direction
Fe_3O_4	iron oxide
GFRP	glass fiber reinforced polymer
h	height
P	applied load
$R_{a,2}$	arithmetic mean height in the transverse direction
S_{ku}	kurtosis
S_q	root mean square height
S_v	maximum height of valleys
SBT	Simple Beam Theory
σ_{fail}	failure strength
σ_{Yield}	yield strength
TEPs	thermally expandable particles
TMA	thermo-mechanical analyzer

References

[1] Mulcahy, K. R.; Kilpatrick, A. F. R.; Harper, G. D. J.; Walton, A.; Abbott, A. P. Debondable Adhesives and Their Use in Recycling. Green Chem. 2022, *24*(1), 36–61. DOI: 10.1039/d1gc03306a.

[2] MORPHO H2020 – Embedded Life-Cycle Management for Smart Multimaterials Structures: Application to Engine Components. https://morpho-h2020.eu/ (accessed Feb. 11, 2023).

[3] Jairaja, R.; Naik, G. N. Weak Bond Effects in Adhesively Bonded Joints Between the Dissimilar Adherends. *J. Adhes.* 2021, *97*(8), 760–782. DOI: 10.1080/00218464.2019.1702027.

[4] Two Boeing 787 Dreamliners are already being scrapped | CNN Travel."|"Two Boeing 787 Dreamliners are already being scrapped | CNN Travel. https://edition.cnn.com/travel/article/10-year-old-boeing-787s-scrapped/index.html (accessed Apr. 7, 2023).
[5] Bin Anwar, T.; Lewis, T. N.; Berges, A. J.; Gately, T. J.; Bardeen, C. J. Nanosecond Laser Debonding of Strong Adhesives. *J. Adhes*. 2023. DOI: 10.1080/00218464.2023.2211011.
[6] Zhao, B.; Hardiman, M.; Ryan, K. M.; O'Reilly, E.; McCarthy, C. Formation of Reworkable Nanocomposite Adhesives by Dielectric Heating of Epoxy Resin Embedded Fe3O4 Hollow Spheres. *CrystEngcomm*. 2016, *18*(32), 6096–6101. DOI: 10.1039/c6ce01359g.
[7] Sánchez-Romate, X. F.; Del Bosque, A.; Crespo, A.; Alonso, R.; Sánchez, M.; Ureña, A. Fe3O4-Nanoparticle-Doped Epoxy Resin as a Detachable Adhesive by Electromagnetic Heating for GFRP Single-Lap Joints. *Nanomaterials*. 2022, *12*(21), 3913. DOI: 10.3390/nano12213913.
[8] Piazza, G.; Burczyk, M.; Gerini-Romagnoli, M.; Belingardi, G.; Nassar, S. A. Effect of Thermally Expandable Particle Additives on the Mechanical and Reversibility Performance of Adhesive Joints. *J. Adv. Joining Proc*. 2022, Jun, *5*. DOI: 10.1016/j.jajp.2021.100088.
[9] Cheng, X.; Zhou, Y.; Charles, A. D. M.; Yu, Y.; Islam, M. S.; Peng, S.; Wang, J.; Rider, A. N.; Lim, M.; Timchenko, V., et al. Enabling Contactless Rapid On-Demand Debonding and Rebonding Using Hysteresis Heating of Ferrimagnetic Nanoparticles. *Mater. Des*. 2021, *210*, 110076. DOI: 10.1016/j.matdes.2021.110076.
[10] Kanidi, M.; Loura, N.; Frengkou, A.; Milickovic, T. K.; Trompeta, A. F.; Charitidis, C. Inductive Thermal Effect on Thermoplastic Nanocomposites with Magnetic Nanoparticles for Induced-Healing, Bonding and Debonding On-Demand Applications. *J. Compos. Sci*. 2023, *7*(2). DOI: 10.3390/jcs7020074.
[11] He, Z.; Luo, Q.; Li, Q.; Zheng, G.; Sun, G. Fatigue Behavior of CFRP/Al Adhesive Joints — Failure Mechanisms Study Using Digital Image Correlation (DIC) Technique. *Thin-Walled Struct*. 2022, *174*, (September 2021), 109075. DOI: 10.1016/j.tws.2022.109075.
[12] Yuan, Y.; Zhang, Q.; Li, X.; Wuyun, Q.; Zhang, Z. Effective Method for Measuring Shear Nonlinearity of Nanocomposites Using Digital Image Correlation. *J. Nondestr. Eval*. 2021, *40*(3), 1–11. DOI: 10.1007/s10921-021-00790-w.
[13] Sun, F.; Zhang, R.; Blackman, B. R. K. Determination of the Mode I Crack Tip Opening Rate and the Rate Dependent Cohesive Properties for Structural Adhesive Joints Using Digital Image Correlation. *Int. J. Solids Struct*. 2021, *217-218*, 60–73. DOI: 10.1016/j.ijsolstr.2021.01.034.
[14] Sun, G.; Liu, X.; Zheng, G.; Gong, Z.; Li, Q. On Fracture Characteristics of Adhesive Joints with Dissimilar Materials - an Experimental Study Using Digital Image Correlation (DIC) Technique on Fracture Characteristics of Adhesive Joints with Dissimilar Materials – an Experimental Study Using Digit, No. *June*. 2018. DOI: 10.1016/j.compstruct.2018.06.018.
[15] Bai, R.; Bao, S.; Lei, Z.; Yan, C.; Han, X. Finite Element Inversion Method for Interfacial Stress Analysis of Composite Single-Lap Adhesively Bonded Joint Based on Full-Field Deformation. *Int. J. Adhes. Adhes*. 2018, *81*, (September 2021), 48–55. DOI: 10.1016/j.ijadhadh.2017.11.011.
[16] Iron Oxide Nanopowder/Nanoparticles (Fe3O4, high purity, 99.5+%, 15-20 nm). https://www.us-nano.com/inc/sdetail/435 (accessed Aug. 8, 2022).
[17] Li, Q.; Kartikowati, C. W.; Horie, S.; Ogi, T.; Iwaki, T.; Okuyama, K. Correlation Between Particle Size/Domain Structure and Magnetic Properties of Highly Crystalline Fe3O4 Nanoparticles. *Sci. Rep*. 2017, *7*(1), 1–4. DOI: 10.1038/s41598-017-09897-5.

[18] Lenin, N.; Karthik, A.; Sridharpanday, M.; Selvam, M.; Srither, S. R.; Arunmetha, S.; Paramasivam, P.; Rajendran, V. Electrical and Magnetic Behavior of Iron Doped Nickel Titanate (Fe3+/NiTio3) Magnetic Nanoparticles. *J. Magn. Magn. Mater*. 2016, *397* (January), 281–286. DOI: 10.1016/j.jmmm.2015.08.115.
[19] Scotch-Weld ™ EPX ™ Adhesive DP490.
[20] Srinivasan, D. V.; Ravichandran, V.; Idapalapati, S. Failure Analysis of GFRP Single Lap Joints Tailored with a Combination of Tough Epoxy and Hyperelastic Adhesives. *Compos. Part B*. 2020, *200*(June), 108255. DOI: 10.1016/j.compositesb.2020.108255.
[21] Caglar, H.; Idapalapati, S.; Sharma, M.; Sin, K. Debonding of Carbon Fiber Veil Interleaved Adhesively Bonded GFRP Joints via Joule Heating. *Compos. Part B*. 2022, *230*, (July 2021), 109544. DOI: 10.1016/j.compositesb.2021.109544.
[22] Caglar, H.; Idapalapati, S.; Sharma, M.; Sin, C. K. Debonding of Bonded Composite Joints with TEP Modified Epoxy Adhesives. *J. Adhes*. 2022, 99 (10), 1–24. DOI: 10.1080/00218464.2022.2152333.
[23] ASTM Standard D3433-99. Standard Test Method for Fracture Strength in Cleavage of Adhesives in Bonded Metal Joints. *ASTM int*. 2012, *99*,(Reapproved), 3.
[24] Astm. ASTM D638: Standard Test Method for Tensile Properties of Plastics. *ASTM Standards*; January, 2004.
[25] ASTM E8. ASTM E8/E8M Standard Test Methods for Tension Testing of Metallic Materials 1. *Annu. B. ASTM Standard*. 2010, *4*(C), 1–27. DOI:10.1520/E0008.
[26] He, Y.; Chen, Q.; Yang, S.; Lu, C.; Feng, M.; Jiang, Y.; Cao, G.; Zhang, J.; Liu, C. Micro-Crack Behavior of Carbon Fiber Reinforced Fe3O4/Graphene Oxide Modified Epoxy Composites for Cryogenic Application. *Compos. Part A Appl. Sci. Manuf*. 2018, *108*, (December 2017), 12–22. DOI: 10.1016/j.compositesa.2018.02.014.
[27] Li, G.; Fei, W. D. Abnormal Thermal Expansion Behavior of Aluminum Borate Whisker Reinforced Aluminum Composite Containing Fe3O4 Particles. *Mater. Chem. Phys*. 2006, *99*(1), 34–38. DOI: 10.1016/j.matchemphys.2005.09.050.
[28] Jouyandeh, M.; Jazani, O. M.; Navarchian, A. H.; Shabanian, M.; Vahabi, H.; Saeb, M. R. Bushy-Surface Hybrid Nanoparticles for Developing Epoxy Superadhesives. *Appl. Surf. Sci*. 2019, *479*. DOI: 10.1016/j.apsusc.2019.01.283.
[29] Shabeer, A.; Garg, A.; Sundararaman, S.; Chandrashekhara, K.; Flanigan, V.; Kapila, S. Dynamic Mechanical Characterization of a Soy Based Epoxy Resin System. *J. Appl. Polym. Sci*. 2005, *98*(4), 1772–1780. DOI: 10.1002/app.22362.
[30] Jouyandeh, M.; Paran, S. M. R.; Shabanian, M.; Ghiyasi, S.; Vahabi, H.; Badawi, M.; Formela, K.; Puglia, D.; Saeb, M. R. Curing Behavior of Epoxy/Fe3O4 Nanocomposites: A Comparison Between the Effects of Bare Fe3O4, Fe3O4/SiO2/Chitosan and Fe3O4/SiO2/chitosan/imide/phenylalanine-Modified Nanofillers. *Prog. Org. Coat*. 2018, *123* (June), 10–19. DOI: 10.1016/j.porgcoat.2018.06.006.
[31] Vattathurvalappil, S. H.; Haq, M.; Kundurthi, S. Hybrid Nanocomposites—An Efficient Representative Volume Element Formulation with Interface Properties. *Polym. Polym. Composites*. 2022, *30*. DOI: 10.1177/09673911221084651.
[32] Voβ, M.; Vallée, T. Effects of Curie Particle Induced Accelerated Curing on Thermo Mechanical Performance of 2K Structural Adhesives–Part I: Bulk Properties. *J. Adhes*. 2021, *98*(9), 1–42. DOI: 10.1080/00218464.2021.1909482.
[33] Apalak, M. K.; Gunes, R. On Non-Linear Thermal Stresses in an Adhesively Bonded Single Lap Joint. *Comput. Struct*. 2002, *80*(1), 85–98. DOI: 10.1016/S0045-7949(01)00139-0.
[34] Blackman, B. R. K.; Hadavinia, H.; Kinloch, A. J.; Paraschi, M.; Williams, J. G. The Calculation of Adhesive Fracture Energies in Mode I: Revisiting the Tapered Double

Cantilever Beam (TDCB) Test. *Eng. Fract. Mech.* 2003, *70*(2), 233–248. DOI: 10.1016/S0013-7944(02)00031-0.

[35] Buchman, A.; Dodiuk-Kenig, H.; Dotan, A.; Tenne, R.; Kenig, S. Toughening of Epoxy Adhesives by Nanoparticles. *J. Adhes. Sci. Technol.* 2009, *23*(5), 753–768. DOI: 10.1163/156856108X379209.

[36] Er Wang, X.; Pang, K.; Huang, X.; Yang, J.; Ye, J.; Hou, X. Insights into the Micromechanical Response of Adhesive Joint with Stochastic Surface Micro-Roughness. *Eng. Fract. Mech.* 2023, *277*, (August 2022), 108954. DOI: 10.1016/j.engfracmech.2022.108954.

[37] Demirci, S.; Dikici, T.; Güllüoğlu, A. N. Micro/Nanoscale Surface Modification of Ti6Al4V Alloy for Implant Applications. *J. Mater. Eng. Perform.* 2022, *31*(2), 1503–1511. DOI: 10.1007/s11665-021-06232-y.

[38] Costa, M. Y. P.; Venditti, M. L. R.; Voorwald, H. J. C.; Cioffi, M. O. H.; Cruz, T. G. Effect of WC-10%co-4%cr Coating on the Ti-6Al-4V Alloy Fatigue Strength. *Mater. Sci. Eng. A.* 2009, *507*(1–2), 29–36. DOI: 10.1016/j.msea.2008.11.068.

[39] Lane, B.; Sherratt, P.; Hu, X.; Harland, A. Measurement of Strain and Strain Rate During the Impact of Tennis Ball Cores. *Appl. Sci. (Switzerland).* 2018, *8*(3). DOI: 10.3390/app8030371.

[40] Kellar, E. J. C. Joining Similar and Dissimilar Materials. *Adhesive Bonding: Science, Technology And Applications.* 2021. DOI: 10.1016/B978-0-12-819954-1.00004-6.

[41] Seong, M. S.; Kim, T. H.; Nguyen, K. H.; Kweon, J. H.; Choi, J. H. A Parametric Study on the Failure of Bonded Single-Lap Joints of Carbon Composite and Aluminum. *Compos. Struct.* 2008, *86*(1–3). DOI: 10.1016/j.compstruct.2008.03.026.

[42] Kafkalidis, M. S.; Thouless, M. D. The Effects of Geometry and Material Properties on the Fracture of Single Lap-Shear Joints. *Int. J. Solids. Struct.* 2002, *39*(17). DOI: 10.1016/S0020-7683(02)00344-X.

[43] Sokolinsky, V. S.; Indermuehle, K. C.; Hurtado, J. A. Numerical Simulation of the Crushing Process of a Corrugated Composite Plate. *Compos. Part A Appl. Sci. Manuf.* 2011, *42*(9). DOI: 10.1016/j.compositesa.2011.04.017.

[44] Yang, X.; Yao, L.; Xia, Y.; Zhou, Q. Effect of Base Steels on Mechanical Behavior of Adhesive Joints with Dissimilar Steel Substrates. *Int. J. Adhes. Adhes.* 2014, *51*. DOI: 10.1016/j.ijadhadh.2014.02.010.

[45] Bayerl, T.; Duhovic, M.; Mitschang, P.; Bhattacharyya, D. The Heating of Polymer Composites by Electromagnetic Induction - a Review. *Compos. Part A Appl. Sci. Manuf.* 2014, *57*(2014), 27–40. DOI: 10.1016/j.compositesa.2013.10.024.

[46] Severijns, C.; de Freitas, S. T.; Poulis, J. A. Susceptor-Assisted Induction Curing Behaviour of a Two Component Epoxy Paste Adhesive for Aerospace Applications. *Int. J. Adhes. Adhes.* 2017, *75*, 155–164. DOI: 10.1016/j.ijadhadh.2017.03.005.

[47] Qian, L.; Peng, J.; Xiang, Z.; Pan, Y.; Lu, W. Effect of Annealing on Magnetic Properties of Fe/Fe3O4 Soft Magnetic Composites Prepared by in-Situ Oxidation and Hydrogen Reduction Methods. *J. Alloys Compd.* 2019, *778*, 712–720. DOI: 10.1016/j.jallcom.2018.11.184.

[48] Rudnev, V.; Loveless, D.; Cook, R. L. *Handbook Of Induction Heating.* 2017. DOI: 10.1201/9781315117485.